Original

Riedel, M.; Gustschin, A.; Ushakov, L.; Noichl, W.; Taphorn, K.; Busse, M.; Beckmann, F.; Hammel, J.; Moosmann, J.; Herzen, J.:
High-resolution quantitative phase-contrast x-ray imaging for biomedical samples at PETRA III.
In: Proc. SPIE : Developments in X-Ray Tomography XIII. Vol. 11840 2021. 118400W.

First published online by SPIE: 09.09.2021

https://dx.doi.org/10.1117/12.2594506

PROCEEDINGS OF SPIE

SPIEDigitalLibrary.org/conference-proceedings-of-spie

High-resolution quantitative phase-contrast x-ray imaging for biomedical samples at PETRA III

Riedel, Mirko, Gustschin, Alex, Ushakov, Lev, Noichl, Wolfgang, Taphorn, Kirsten, et al.

Mirko Riedel, Alex Gustschin, Lev Ushakov, Wolfgang Noichl, Kirsten Taphorn, Madleen Busse, Felix Beckmann, Jörg Hammel, Julian Moosmann, Pierre Thibault, Julia Herzen, "High-resolution quantitative phase-contrast x-ray imaging for biomedical samples at PETRA III," Proc. SPIE 11840, Developments in X-Ray Tomography XIII, 118400W (9 September 2021); doi: 10.1117/12.2594506

SPIE.

Event: SPIE Optical Engineering + Applications, 2021, San Diego, California, United States

High-resolution quantitative phase-contrast X-ray imaging for biomedical samples at PETRA III

Mirko Riedel[a,b,c], Alex Gustschin[a,b], Lev Ushakov[a,b], Wolfgang Noichl[a,b], Kirsten Taphorn[a,b], Madleen Busse[a,b], Jörg Hammel[c], Julian Moosmann[c], Pierre Thibault[d], Felix Beckmann[c], and Julia Herzen[a,b]

[a]Chair of Biomedical Physics, Department of Physics, School of Natural Sciences, Technical University of Munich, 85748 Garching, Germany
[b]Munich School of BioEngineering, Technical University of Munich, 85748 Garching, Germany
[c]Institute for Materials Physics, Helmholtz-Zentrum Hereon, Max-Planck-Str. 1, 21502 Geesthacht, Germany
[d]Department of Physics, University of Trieste, Trieste 34217, Italy

ABSTRACT

Phase-contrast computed tomography enables visualizing soft tissue samples with high contrast. At the same time, typically used phase-retrieval techniques often compromise resolution or phase sensitivity. In order to increase the resolution for quantitative phase-contrast measurements, we built a new speckle-based imaging setup at the beamline P05 at Petra III / DESY. By exchanging the wavefront marker with a 2D phase grating as wavefront marker, we improved the visibility allowing for faster scan acquisition. We developed a post processing chain which is able to compensate wavefront marker vibrations and tested the setup capabilities and resolution at different phase-retrieval settings. The setup was able to successfully image biomedical samples at a resolution up to 2.1 µm. By doing so, a resolution level close to the system resolution and comparable to propagation based imaging is reached, while at the same time no assumptions about the sample are made and quantitative electron density information can be accessed.

Keywords: Phase-contrast, Speckle-Based Imaging, X-ray Tomography

1. INTRODUCTION

Multiple imaging methods have been proposed and are in use to visualize the phase-shifting properties of an object on a microscopic level. Today's most common methods at synchrotron sources include the propagation-based imaging (PBI) techniques,[1] the grating-based imaging techniques (GBI)[2] and, as a most recent addition, the speckle-based imaging (SBI) techniques.[3,4] Their difference lies in the setup complexity, phase sensitivity, and application area. PBI techniques are comparably simple to implement into an existing setup. If certain assumptions about the sample are possible, like the sample is made of a single material or weakly absorbing, the phase can be recovered by a single measurement.[5] However, if these assumptions are not applicable, the phase retrieval becomes more complex. In contrast, differential methods like GBI do not require any assumptions about the sample. Their disadvantages usually lie in their setup complexity or their influence on the spatial resolution. In recent years, SBI was introduced as an additional differential phase-contrast method. As more and more speckle tracking algorithms were added, SBI can be seen as a general term for phase-contrast methods using a strongly modulated wavefront. While implicit tracking methods[6,7] are more related to PBI, explicit methods[8,9] rely on correlation analysis to retrieve the imaging signals and are part of the differential phase-contrast methods. For biomedical imaging, all of the methods mentioned above are in use. The choice of the suitable setup often depends on multiple parameters. Setup-dependent properties, like complexity, the measurement time, and the computational effort for phase retrieval, differ and have to be considered during the design of an experiment. The exact question on a sample can also require or exclude certain methods, as spatial resolution, phase sensitivity

Further author information:
Mirko Riedel: E-mail: mirko.riedel@tum.de

Developments in X-Ray Tomography XIII, edited by Bert Müller
Ge Wang, Proc. of SPIE Vol. 11840, 118400W · © 2021 SPIE
CCC code: 0277-786X/21/$21 · doi: 10.1117/12.2594506

and the ability to gather quantitative information about the sample are dependent on the method. While PBI delivers high-resolution scans, its sensitivity is lower, compared to the differential phase-contrast techniques.[10,11] GBI setups can lower the spatial resolution, while on the other hand being able to provide quantitative phase information. For SBI the properties depend on the choice of the tracking algorithm. With the latest addition to explicit speckle tracking algorithms, the Unified Modulated Pattern Analysis (UMPA), SBI has shown its application possibilities for phase-contrast CT at a high resolution.[12]

In order to obtain quantitative phase information at a spatial resolution level close to the system resolution we designed and constructed a new setup at the Imaging Beamline P05 at PETRA III. In this work, we determined the relevant setup characterization parameters and demonstrate its feasibility for first applications on biological samples.

2. MATERIALS AND METHODS

2.1 Sample Preparation

During this work, two samples were investigated. As a first sample, a mouse kidney was scanned. The animal housing and organ removal was carried out at the Klinikum rechts der Isar, Technical University of Munich in accordance with the European Union guidelines 2010/63 and with approval from an internal animal protection committee of the Center for Preclinical Research of Klinikum rechts der Isar, Munich, Germany (internal reference number 4-005-09). After removal, the sample was fixated in a formaldehyde solution and stained with a bismuth-oxo-cluster.[13] After a dehydration series, the stained sample was embedded in paraffin wax and mounted for scanning. The second sample, a section of human kidney tissue, was provided by the Institute of Forensic Medicine, Ludwig-Maximilians-Universität München under an institutional ethics approval (151-08). The sample was again fixated in a formaldehyde solution, dehydrated, and embedded in paraffin, with no staining.

2.2 Data Acquisition

The setup was designed at the micro-tomography end-station of the imaging beamline P05 at PETRA III.[14] An undulator source, in combination with a double crystal monochromator, was used to provide a monochromatic beam with a photon energy of 20 keV. As camera, a Ximea CB500MG with a CMOSIS CMV50000 sensor was used, with a physical pixel size of 4.6 µm. The field of view at five-fold magnification is limited in height by the beam height to approx. 3 mm, the maximum width at this magnification is 7.29 mm. The resolution of the detector system is limited by the microscope optics to approx. 1 µm.
The wavefront marker was adapted to use a 2D phase-shifting grating, a so-called Talbot Array Illuminator (TAI)[15,16] instead of sandpaper. The grating had a period of 10 µm, a duty cycle of $DC = 1/3$, and a phase shift of $\phi = \frac{2\pi}{3}$. At fractional Talbot distances of $\frac{1}{6}d_T$ these TAIs show a focusing effect with a theoretical compression ratio of 1:3 in each direction, thus a high visibility can be achieved. By using TAIs as wavefront markers, absorptive elements were avoided and an efficient two-dimensional stepping could be embodied. The periodic nature of such gratings implies an ideal, regular stepping scheme, using a square number of wavefront marker positions. Stepping was performed using a 2D piezo stepper motor which was mounted onto the detector granite structure.
The samples were mounted on an air-bearing rotation stage in between the wavefront marker and the detector. The optimal fractional Talbot distance for the 10 µm grating used, would be at 538 mm. However, due to setup limitations, the grating cannot be placed arbitrarily far in front of the sample. At the same time, long propagation distances from the sample to the detector causes strong edge enhancement effects, disturbing the phase retrieval and creating artifacts. In order to avoid this, the detector is moved closer to the sample and the grating. This causes a slight loss of visibility of the gratings, which was determined at approx. 0.5.
The scans are recorded using a continuous rotation mode. Multiple wavefront marker steps are realized by recording multiple scans, with changing the wavefront marker position in between the scans. A set of around 100 flat-field images are taken at the beginning and the end of each scan.
The first scanned sample was the stained mouse kidney. Due to the stain, a single distance propagation-based phase-contrast scan did not yield satisfying results and therefore our developed protocol was chosen to visualize this sample. The tomography of the mouse kidney was performed at a beam energy of 20 keV with 2001

projections over 180 degrees. The propagation distance was chosen at 160 mm and 16 wavefront marker positions were imaged, with an exposure time of 80 ms per image. The detector used a 100 µm $CdWO_4$ scintillator screen and a five-fold magnification objective, resulting in an effective pixel size of 0.92 µm. The scan was then processed and evaluated for varying UMPA window sizes between 1x1 and 25x25 pixel
The second scan of the human kidney tissue was optimized for a high spatial resolution. A thinner scintillator screen was mounted, 30 µm LuAG. At the same time, a ten-fold magnification objective was used, resulting in an effective pixel size of 0.46 µm. In order to increase the width of the field of view, the rotation axis was shifted by 2500 pixels from the center, and projections were acquired over 360 degrees. A total of 5000 projections of a human kidney sample were taken per scan, at an exposure time of 200 ms with 16 wavefront marker positions and a propagation distance of 180 mm.

2.3 Data Processing

The acquired images were corrected for the camera dark-current and intensity fluctuations of the beam. As SBI requires the reference images to be taken at precisely the same wavefront marker position as the sample projections, a correction for wavefront marker vibrations was required. For this, a principal component analysis was performed on the flat-field images of each grating position f_j.[17] This yields several so-called Eigenflat-field images u_k and their corresponding Eigenvalues. By using a scree plot, the relevant N components, typically around 15, were chosen and the remaining were discarded.
In order to generate a best-fitting reference image at an unknown position and therefore to correct for wavefront marker vibrations, a new reference image f_n can be expressed by a weighted sum over the relevant components:

$$f_n = \bar{f}_j + \sum_{k=1}^{N} w_k \cdot u_k. \tag{1}$$

Suitable weights were selected by taking a background region of each projection p_{BG} and performing a least-squares fit using the Eigenflat-field images:

$$w_k = \arg\min_{w_k} \left(p_{BG} - f_{n,BG}\right)^2. \tag{2}$$

The resulting weights were used to generate the reference image according to eq. 1. The conventional absorption image was calculated from the mean over all phase steps.
Afterward, phase-retrieval was performed on the projection images by using the Unified Modulated Pattern Analysis (UMPA).[9] The resulting differential phase images were corrected for ramps and outliers, anti-symmetric mirrored,[18] and integrated, using a Fourier approach.[19] The integrated phase was filtered for ring artifacts and reconstructed via filtered back-projection and a Ram-Lak filter using the software X-Aid (Mitos GmbH, Garching, Germany).

2.4 Data Evaluation

The angular sensitivity, corresponding to the smallest resolvable refraction angle was obtained from the standard deviation in a background region of the differential phase images. The electron density resolution in the reconstructed slices was estimated from the standard deviation of the noise in a homogeneous material.
In order to determine the spatial resolution of the reconstructed slices, multiple edges in the image were chosen and an error function was fitted. As a resolution criterion, the FWHM of the associated Gaussian of the ERFC can be used, which corresponds to approx. FWHM $\approx 1.178\,\sigma$.
A determination of the resolution by analyzing the Fourier power spectrum can be performed by calculating the 2D Fourier transform of an ROI and taking the azimuthal average. The resolution level is defined as twice the noise level in the image. The latter can be determined by taking the highest occurring frequencies. A fourth-order polynomial is fitted to the FPS to find the intersection with twice the noise level.[20]
This method is only limited applicable to UMPA phase retrieved images. The window function in the phase-retrieval process blurs the noise as well as the features. This blur can result in underestimation of the resolution, especially at large window sizes. The resolution is determined to be more or less independent of the window. Modregger et al. already suggest, that filtering the Fourier power spectrum does not change the outcome, as noise and features are filtered approximately equally.

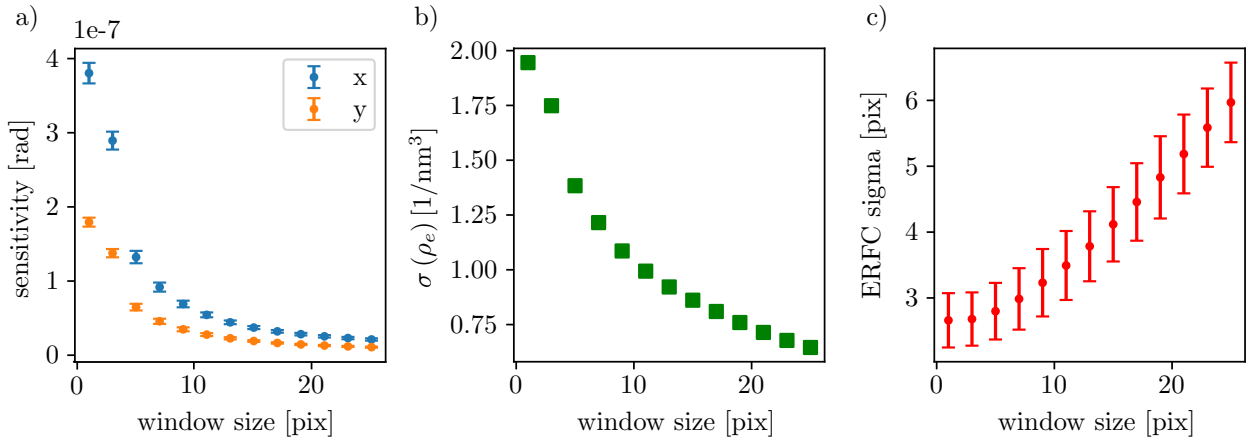

Figure 1. In **a)** the mean sensitivity in x and y direction over all projections of the scan is shown as function of the UMPA window size. The error bars mark the standard deviation. Plot **b)** shows the electron density resolution in the reconstructed slices as function of the UMPA window. In **c)** the mean sigma values of error function (ERFC) fits to edges in the images are depicted. As resolution criterion the FWHM of the associated Gaussian function can be used, corresponding to $FWHM \approx 1.178\sigma$.

3. RESULTS AND DISCUSSION

3.1 Mouse Kidney

3.1.1 Angular Sensitivity in Projections

The differential phase projections were evaluated for their angular sensitivity in x and y direction depending on the UMPA window sizes. This was calculated for each projection and the mean for each window size is depicted in fig. 1 **a)**. For the smallest window size, the minimum resolvable refractive angle is the largest. With increasing window size, smaller lateral shifts can be detected and the sensitivity improves to lower values.

The angular sensitivity of a UMPA phase retrieved projection is linked to the number of wavefront marker positions N, the UMPA window size w and a setup dependent constant for each direction $C_{x/y}$ by:[9]

$$\sigma_{x/y} = \frac{C_{x/y}}{w\sqrt{N}}. \tag{3}$$

As N was kept constant for all window sizes the root-like behavior on w can be seen. The difference in sensitivity in x and y directions can be attributed to different coherence properties of the beam at synchrotron sources. The beam emittance in the vertical direction is typically several orders of magnitude smaller than in horizontal and therefore the coherence is higher in this direction. Other factors such as system vibration can also have an influence. These factors contribure to the setup constant $C_{x/y}$.
In contrast to the improvement of the smallest resolvable refraction angle, the spatial resolution in projection is decreasing with larger window sizes. The resolution in projection can be estimated as twice the FWHM of the phase-retrieval window. Contrary to the gain in sensitivity, as in eq. 3, the FWHM increases linearly with the window size. This limits the possibility to improve the sensitivity arbitrarily far, as the cost in resolution remains constant.

3.1.2 Reconstructed slices

A tomographic slice, of the electron density distribution of the stained mouse kidney, phase-retrieved using a window of 3x3 pixel is shown in fig. 2. On the left, an overview of the kidney is shown. The different areas, the inner medulla (IM), the outer medulla (OM), and the renal cortex (COR) are marked and can be distinguished by their electron density. The two extracts on the right show the level of detail available. To some extend, ring

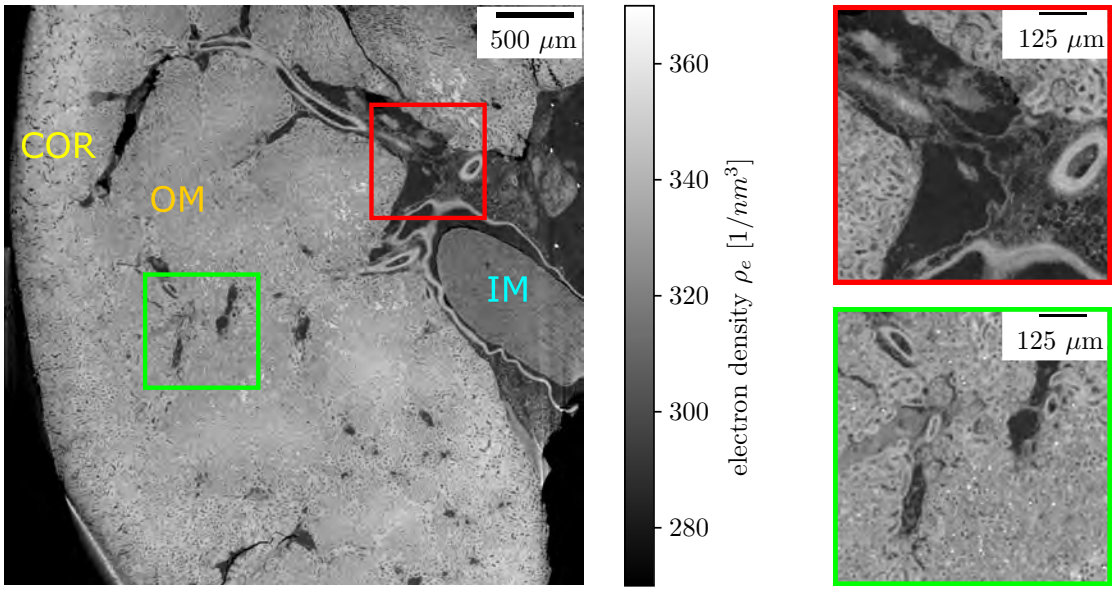

Figure 2. On the left, a reconstructed slice of the stained mouse kidney is shown. The phase retrieval was computed using a window size of 3x3 pixel, the retrieved phase-shift was computed to units of electron density. The effective pixel size is 0.92 µm. The different regions of the kidney, the inner medulla (IM), the outer medulla (OM) and the renal cortex (COR) can be distinguished well. The two zoom-ins show a good level of detail in the tissue.

artifacts as a result of residues of the grating pattern were not fully suppressed and can be seen when zooming in.
The resolution of this slice was determined to be at 3.2 pixel with 2.9 µm respectively, whereas the electron density resolution was determined at $\Delta\rho_e$=1.75 electrons/nm^3.
In the following, this slice was used to compare the effect of the UMPA window size on the data.

Electron density resolution The electron density resolution in the reconstructed slices was evaluated using a homogeneous 40x40x20 pixel ROI of the embedding paraffin wax. The results are shown in fig. 1 **b)**.
The standard deviation is the highest for the smallest window size. With increasing windows, and thus, increasing sensitivity, the electron density resolution improves. As the electron density resolution corresponds to noise in the slices, it is also influenced by factors in the reconstruction process, like binning, different reconstruction filters which suppress high spatial frequencies or additional smoothing.

Spatial resolution The spatial resolution was determined by selecting five edges in a reconstructed CT slice and fitting an error function (ERFC). The resulting sigma values are shown in fig. 1 **c)**. The spatial resolution deteriorates, the larger the window size gets. For small UMPA windows, the improvement in resolution stagnates when decreasing the window. As the setup resolution is larger than one pixel, it proposes a lower limit, below which no further gain in resolution can be achieved by using smaller phase-retrieval windows. As the electron density resolution or noise in the slices does not have this limit, the window size should be chosen close to the resolution limit.
The visual effect of different UMPA window sizes on the reconstruction is compared in fig. 3 for windows of 1x1, 11x11 and 25x25 pixel. The decrease in spatial resolution with an increasing blur in the images can be seen well. Small features get lost for larger windows, while at the same time, remaining artifacts get reduced.
For increasing window sizes, a trend to underestimate the electron density compared to small window sizes becomes visible. This is a result of the increased blurring of differential phase images, which causes an underestimation of the phase shift, particularly at sharp edges of a sample. After phase integration, the resulting phase shift, and thus the local electron density, is estimated lower.

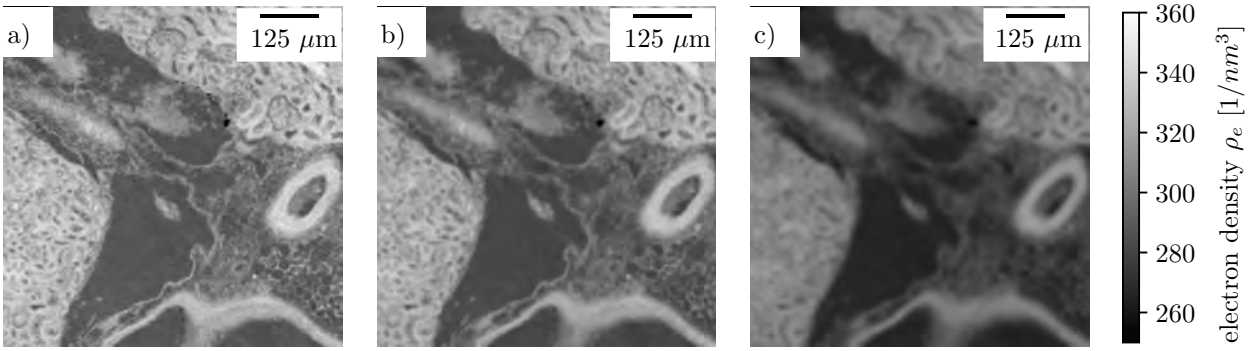

Figure 3. Comparison of different UMPA window sizes. In **a)** a window size of 1x1 pix is shown, in **b)** of 11x11 pix and in **c)** of 25x25 pix. The resolution decreases with larger window sizes as the images get blurred and featues cannot be distinguished any longer. At the same time, the electron density is estimated at lower values for larger window sizes.

3.2 Human Kidney

The scan of the human kidney sample was optimized for high resolution with an extended field of view. The latter one, enables scanning the whole sample, even with the ten-fold magnification objective. The projections were phase retrieved using an UMPA window of 3x3 pixel. Before integration, the overlap of two opposing angles was determined via cross-correlation and the differential images were stitched together. A ROI is shown in fig. 4 on the left.

The resolution of the scan was determined by analyzing edges in the image and by analyzing the Fourier power spectrum. The electron density values of the line indicated in the image are depicted on the top right. An ERFC was fitted and is plotted, as well as the expected value and the standard deviation. This method resulted in a sigma value of σ =1.8 µm and a resolution of 2.1 µm respectively.

For the second method, the Fourier power spectrum of the slice as shown was calculated and azimuthally averaged. A section of this is shown in fig. 4 on the bottom right. The noise level of the slice was determined by taking the mean over the 20 highest frequencies. A fourth-order polynomial was fitted to the area indicated by the gray dashed lines. For the resolution level, the intersection of this fit with twice the noise level was determined. This resulted in a resolution of 728 lp/mm or 1.4 µm respectively. As this resolution determination method does not include the post-processing blur, its values are more of theoretical interest.

3.3 Conclusion

With the design of this setup and by tuning the components and acquisition protocol, it is possible to reach a resolution of 2.1 µm. This is close to the system limit and comparable to the level of PBI. At the same time, the advantages of differential phase-contrast methods, namely the higher sensitivity and quantitative values, are used. With this, it is possible to investigate samples with phase-contrast imaging, without having to make any assumptions about their properties and while still keeping the resolution level of the imaging system.

Our setup is easy to implement and the adaption to use TAIs can provide a higher visibility compared to previously used wavefront markers. In comparison to sandpaper, the visibility is reached after a shorter propagation distance, allowing for a more compact setup. Combined with the regular nature of the grating pattern, the phase-stepping can be optimized so and fewer steps are necessary to reach a good sensitivity. Unlike random wavefront markers, the periodic structure of the gratings can cause problems if phase wrapping is occurring and can therefore hinder increasing the sensitivity arbitrarily. To prevent phase wrapping, the sample can be measured in an embedding medium, to prevent large phase shifts at edges or the propagation distance can be decreased.

We presented a way to correct for wavefront marker position inaccuracies by performing a PCA and using a least-squares fit in a background region. This allows to compensate for small vibrations and increases the image

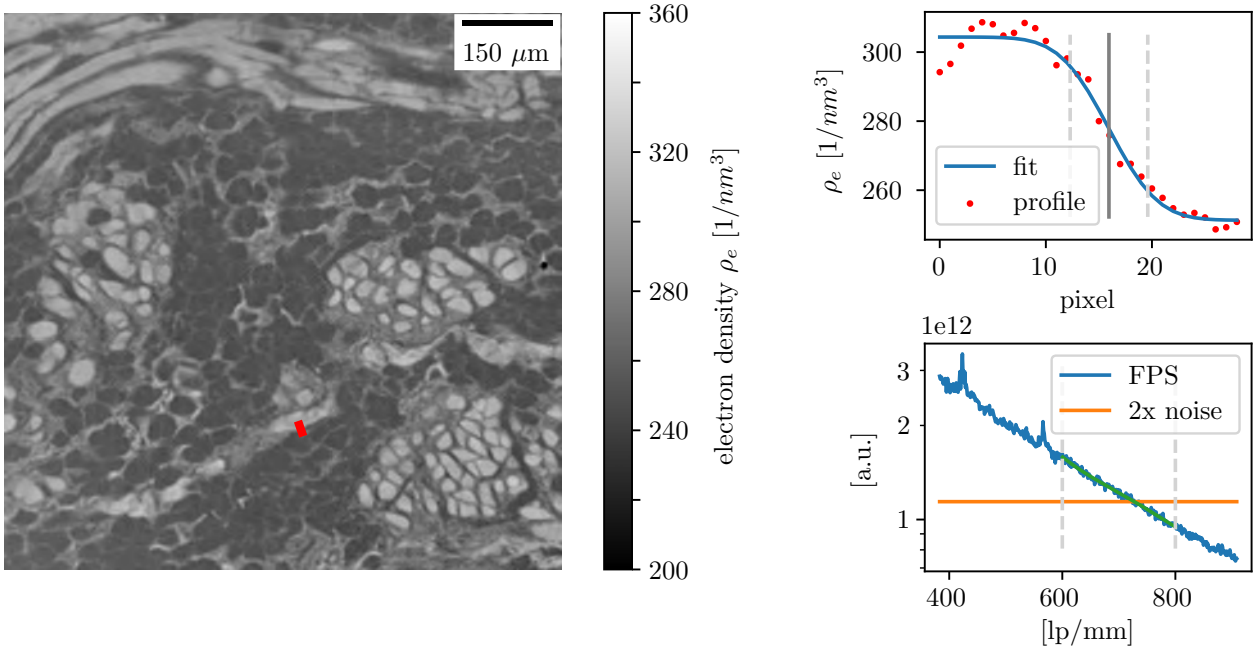

Figure 4. On the left, a reconstructed section of the human kidney is shown. The phase retrieval was computed using a window size of 3x3 pixel, the retrieved phase-shift was computed to units of electron density. The effective pixel size is 0.46 µm. The plot on the top right shows the profile of the line indicated in the picture. An ERFC was fitted and the fit sigma value was used for the resolution criterion. The solid gray line indicates the expected value, the dashed lines the standard deviation. The plot on the bottom right shows a section of the Fourier power spectrum (FPS) of the image. The noise level was determined by taking the mean over the 20 highest frequencies. The resolution was determined by fitting a fourth-order polynomial to the FPS in the area indicated and determining the intersection with the noise level.

quality and sensitivity. The setup sensitivity is tuneable and can be increased by acquiring a larger number of wavefront marker positions during the measurement or by increasing the propagation distance from the sample to the detector and going to higher fractional Talbot orders of the grating. To a certain extent, it is even possible to tune the sensitivity after the measurement by trading in resolution during the phase retrieval.
With the increasing computational power of recent years, the demands of explicit speckle-tracking algorithms can be addressed even for a larger number of scans during a user beamtime.
The setup is flexible in its energy range and has been tested between 15 and 64 keV, addressing a broad class of sample systems, from biomedical to material science samples.

ACKNOWLEDGMENTS

We acknowledge DESY (Hamburg, Germany), a member of the Helmholtz Association HGF, for the provision of experimental facilities. Parts of this research were carried out at PETRA III and we would like to thank Fabian Wilde for assistance in using the Beamline P05, operated by the Helmholz-Zentrum Hereon. Beamtime was allocated for proposal LTP II-20190765. First tests on the Beamline P07 were performed as part of the proposal I-20200511. This research was supported in part through the Maxwell computational resources operated at DESY.

REFERENCES

[1] Gureyev, T. E., Mayo, S. C., Myers, D. E., Nesterets, Y., Paganin, D. M., Pogany, A., Stevenson, A. W., and Wilkins, S. W., "Refracting röntgen's rays: Propagation-based x-ray phase contrast for biomedical imaging," *Journal of Applied Physics* **105**(10), 102005 (2009).

[2] Momose, A., Kawamoto, S., Koyama, I., Hamaishi, Y., Takai, K., and Suzuki, Y., "Demonstration of x-ray talbot interferometry," *Japanese Journal of Applied Physics* **42**(Part 2, No. 7B), L866–L868 (2003).

[3] Bérujon, S., Ziegler, E., Cerbino, R., and Peverini, L., "Two-dimensional x-ray beam phase sensing," *Physical Review Letters* **108**(15) (2012).

[4] Morgan, K. S., Paganin, D. M., and Siu, K. K. W., "X-ray phase imaging with a paper analyzer," *Applied Physics Letters* **100**(12), 124102 (2012).

[5] Paganin, D., Mayo, S. C., Gureyev, T. E., Miller, P. R., and Wilkins, S. W., "Simultaneous phase and amplitude extraction from a single defocused image of a homogeneous object," *Journal of Microscopy* **206**(1), 33–40 (2002).

[6] Paganin, D. M., Labriet, H., Brun, E., and Berujon, S., "Single-image geometric-flow x-ray speckle tracking," *Physical Review A* **98**(5), 053813 (2018).

[7] Pavlov, K. M., Paganin, D. M., Li, H. T., Berujon, S., Rougé-Labriet, H., and Brun, E., "X-ray multi-modal intrinsic-speckle-tracking," *Journal of Optics* **22**(12), 125604 (2020).

[8] Berujon, S. and Ziegler, E., "X-ray multimodal tomography using speckle-vector tracking," *Physical Review Applied* **5**(4), 044014 (2016).

[9] Zdora, M. C., Thibault, P., Zhou, T., Koch, F. J., Romell, J., Sala, S., Last, A., Rau, C., and Zanette, I., "X-ray phase-contrast imaging and metrology through unified modulated pattern analysis," *Phys Rev Lett* **118**(20), 203903 (2017).

[10] Zanette, I., Lang, S., Rack, A., Dominietto, M., Langer, M., Pfeiffer, F., Weitkamp, T., and Müller, B., "Holotomography versus x-ray grating interferometry: A comparative study," *Applied Physics Letters* **103**(24), 244105 (2013).

[11] Ruiz-Yaniz, M., Zanette, I., Sarapata, A., Birnbacher, L., Marschner, M., Chabior, M., Olbinado, M., Pfeiffer, F., and Rack, A., "Hard x-ray phase-contrast tomography of non-homogeneous specimens: grating interferometry versus propagation-based imaging," *J Synchrotron Radiat* **23**(Pt 5), 1202–9 (2016).

[12] Zdora, M.-C., Thibault, P., Kuo, W., Fernandez, V., Deyhle, H., Vila-Comamala, J., Olbinado, M. P., Rack, A., Lackie, P. M., Katsamenis, O. L., Lawson, M. J., Kurtcuoglu, V., Rau, C., Pfeiffer, F., and Zanette, I., "X-ray phase tomography with near-field speckles for three-dimensional virtual histology," *Optica* **7**(9), 1221 (2020).

[13] Andrews, P. C., Busse, M., Junk, P. C., Forsyth, C. M., and Peiris, R., "Sulfonato-encapsulated bismuth (iii) oxido-clusters from bi 2 o 3 in water under mild conditions," *Chemical Communications* **48**(61), 7583–7585 (2012).

[14] Wilde, F., Ogurreck, M., Greving, I., Hammel, J. U., Beckmann, F., Hipp, A., Lottermoser, L., Khokhriakov, I., Lytaev, P., Dose, T., et al., "Micro-ct at the imaging beamline p05 at petra iii," in [*AIP conference Proceedings*], **1741**(1), 030035, AIP Publishing LLC (2016).

[15] Gustschin, A., Riedel, M., Taphorn, K., Petrich, C., Gottwald, W., Noichl, W., Busse, M., Francis, S. E., Beckmann, F., Hammel, J. U., et al., "High resolution and sensitivity bi-directional x-ray phase contrast imaging using 2d talbot array illuminators," *arXiv preprint arXiv:2105.07347* (2021).

[16] Suleski, T. J., "Generation of lohmann images from binary-phase talbot array illuminators," *Applied optics* **36**(20), 4686–4691 (1997).

[17] Van Nieuwenhove, V., De Beenhouwer, J., De Carlo, F., Mancini, L., Marone, F., and Sijbers, J., "Dynamic intensity normalization using eigen flat fields in x-ray imaging," *Opt Express* **23**(21), 27975–89 (2015).

[18] Bon, P., Monneret, S., and Wattellier, B., "Noniterative boundary-artifact-free wavefront reconstruction from its derivatives," *Appl Opt* **51**(23) (2012).

[19] Kottler, C., David, C., Pfeiffer, F., and Bunk, O., "A two-directional approach for grating based differential phase contrast imaging using hard x-rays," *Optics Express* **15**(3), 1175 (2007).

[20] Modregger, P., Lübbert, D., Schäfer, P., and Köhler, R., "Spatial resolution in bragg-magnified x-ray images as determined by fourier analysis," *physica status solidi (a)* **204**(8), 2746–2752 (2007).